

# Resolution and illumination analyses in PSDM: A ray-based approach

ISABELLE LECOMTE, NORSAR, Kjeller, Norway

Prestack depth migration (PSDM) should be the ultimate goal of seismic processing, producing angle-dependant depth images of the subsurface reflectivity. But the expected quality of PSDM images is constrained by many factors. Understanding all of these factors is necessary to improve depth imaging of geologic structures. In all PSDM approaches, e.g., Kirchhoff or wave-equation, migration always includes compensating for wave propagation in the overburden (back propagation, downward continuation, etc.), before focusing back the reflected/diffracted energy at each considered location in depth (imaging). Ideally, we would like to retrieve the reflectivity of the ground as detailed as possible to invert for the elastic parameters. But the waves perceive the reflectivity through "thick glasses," seeing blurred structures, and not necessarily all of them, depending on the illumination. Only a filtered version of the true reflectivity is therefore retrieved. Being able to estimate these filters, the so-called resolution is the key to a better understanding of the imaging results and improving them, either at an early stage by careful survey planning, or, possibly at a later stage, by properly tuning migration parameters. In addition, interpreters should be aware of such effects. The seismic "wave filters" are easily explained and calculated with ray-based approaches. Once obtained, they can also be used to simulate PSDM images. Ultimately, they could be used to compensate (deblurring) for some of the resolution effects.

**Images of point scatterers.** First, I offer an analogy with astronomy by considering some early images from the Hubble space telescope (Figure 1a). The imaging problem in astronomy is much easier than in seismic because of the propagation of light in a rather homogeneous velocity field and imaging of point-scatterer light sources (stars) in a direct transmission mode instead of backscattered energy (reflection/diffraction). However, the concept of resolution is similar in the optical sense (same for photography). A normal Hubble telescope image of a star is rather blurred with a disturbing cross pattern (highlighted with box), when the star should appear as a dot on the image (Figure 1a). This distortion is easily explained by considering the mirror of the telescope and its intrinsic response to point scatterers, the so-called *point-spread function* (PSF). The PSF can be measured optically all over the surface of the mirror without using an image of the stars (Figure 1b). The major problems faced by astronomers in the early days of the Hubble were the improperly polished mirror's irregularities that yielded space-variant PSFs. Although the variations did not seem to be very dramatic, they were sufficiently pronounced to prevent sharpening the images with standard deblurring algorithms. It is only when these PSFs were thoroughly measured and compensated for in a space-variant deconvolution approach that the Hubble images got sharper

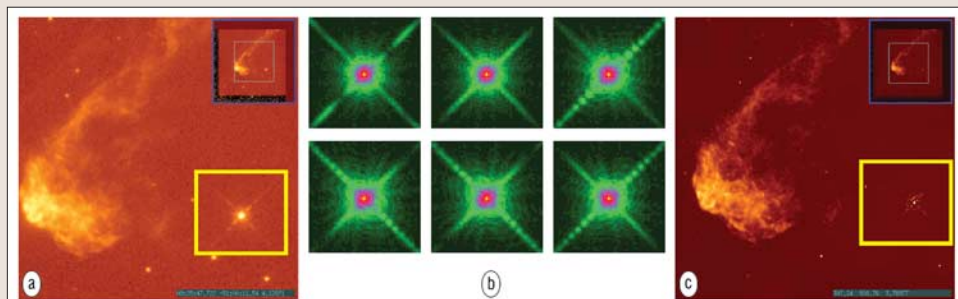


Figure 1. Hubble space telescope. (a) Original distorted image, (b) point-spread functions measured at different locations on the mirror, and (c) PSF-compensated image. From <http://huey.jpl.nasa.gov/mpirl>.

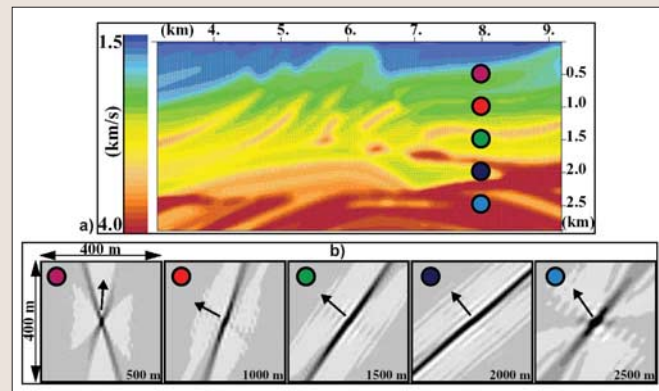


Figure 2. Marmousi model. (a) PSDM background velocity model with five selected locations in depth for one lateral position (colored disks). (b) Calculated PSF at each of the five selected locations for a 5–60 Hz frequency band and an incidence angle range of 0–10°.

(Figure 1c). This example shows how the PSF of an imaging system relates to the quality of the final image, and that it is also possible to compensate for some of the blurring and distortion effects once the PSFs are known.

In seismic and for subsurface structures, the imaging problem is far more complicated because the background velocity field is unknown and often very complex, and we only get information in a backscattering mode. A significant variation in calculated PSFs in the Marmousi model for a few points at one lateral position and at different depths is obvious and challenging (Figure 2). I will show how to calculate these PSFs and how they relate to the final PSDM images. It is important to be able to calculate the PSF rather than using general rules of thumb about resolution. It is often mentioned that the greatest achievable resolution is about a quarter of the wavelength,  $\lambda/4$ , i.e., two near reflectors will be distinguished from each other if the distance between them is equal to or larger than  $\lambda/4$ . We speak here about "vertical resolution" (one should instead speak of cross-reflector resolution), while "lateral resolution" (not necessarily horizontal) is dependent on the Fresnel zone. But these general rules do not help when faced with a complex velocity model where a numerical approach is necessary to properly take into account all effects including acquisition geometry, velocity model, pulse, wave type, etc.

**Inversion.** Before discussing further the concept of resolution in PSDM, let me first define what resolution means here. In the following, the term *resolution* is used in its “inversion-problem” sense: i.e., the resolution of the model parameters of an imaging problem that can be calculated independently from any measured or synthetic data. This is easily explained by writing elementary equations for modeling (Equation 1, forward problem) and imaging (Equation 2, inverse problem) (Menke, 1989):

$$\mathbf{d}^{\text{obs}} = \mathbf{G}\mathbf{m}^{\text{true}} \quad (1)$$

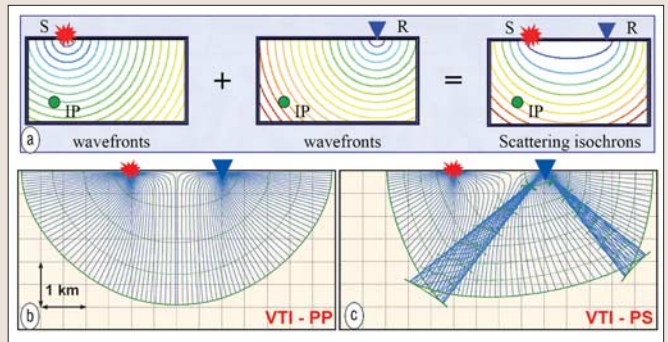
$$\mathbf{m}^{\text{est}} = \mathbf{G}^{-\text{g}}\mathbf{d}^{\text{obs}} \quad (2)$$

In Equation 1,  $\mathbf{d}^{\text{obs}}$  represents observed data (seismic traces),  $\mathbf{G}$  is the Earth model that we assume fits these data, and  $\mathbf{m}^{\text{true}}$  are the actual or “true” model parameters (reflectivity) we would like to retrieve from the data. In Equation 2, a so-called “generalized inverse,”  $\mathbf{G}^{-\text{g}}$  has been calculated and is applied to  $\mathbf{d}^{\text{obs}}$  to obtain an *estimate* of the model parameters  $\mathbf{m}^{\text{est}}$ .  $\mathbf{G}^{-\text{g}}$  is indeed seldom the true inverse  $\mathbf{G}^{-1}$  of  $\mathbf{G}$ , which explains why we cannot retrieve the true model parameters  $\mathbf{m}^{\text{true}}$ , but only an estimate  $\mathbf{m}^{\text{est}}$ . Replacing  $\mathbf{d}^{\text{obs}}$  in inversion Equation 2 by its modeling expression (Equation 1) leads to:

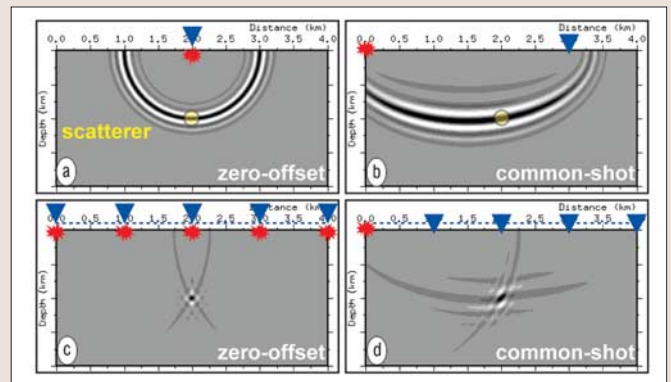
$$\mathbf{m}^{\text{est}} = \mathbf{G}^{-\text{g}}\mathbf{G}\mathbf{m}^{\text{true}} = \mathbf{R}\mathbf{m}^{\text{true}} \quad (3)$$

where  $\mathbf{R} = \mathbf{G}^{-\text{g}}\mathbf{G}$  is the *model resolution* matrix.  $\mathbf{R}$  depends only on  $\mathbf{G}$  and  $\mathbf{G}^{-\text{g}}$ , i.e., it is totally independent of any data, observed or modeled.  $\mathbf{R}$  can therefore be calculated prior to any inversion and is intrinsic to the inversion problem, as are the PSFs measured on the mirror of the Hubble telescope. What matters is the chosen model  $\mathbf{G}$  and its generalized inverse  $\mathbf{G}^{-\text{g}}$ . To come back to our PSDM problem, this means that the term *resolution*, as used in the present paper, will not deal with the possible mismatch of the data  $\mathbf{d}^{\text{obs}}$  with the chosen model  $\mathbf{G}$  (background velocity model), i.e., poor focusing of the seismic energy caused by a wrong propagation model. One can easily obtain cases where the resolution is excellent, while the imaging result will be poor because of the wrong velocity model, hence defocusing. Similarly, a correct velocity model will not by itself ensure good images because other effects such as limited survey aperture, coarse acquisition sampling, frequency-band-limited signals, and the wave propagation itself in complex models will also constrain the resolution, as will be seen.

**Scattering isochrones.** To better understand what happens in PSDM, let us start with the elementary problem of imaging point scatterers, similar to the imaging of stars with the Hubble telescope. However, our seismic “stars” are reflection and diffraction points in the subsurface, acting as secondary sources when first illuminated by a seismic source. We first need a background velocity field to compensate for wave propagation effects between sources and receivers down to each image point. The most important information needed for migration is traveltime, i.e., the migration process must be able to locate back in depth backscattered energy recorded in time. For a given source/receiver pair SR, Figure 3a illustrates the traveltime information from both source S (traveltime  $t_S$ ) and receiver R (traveltime  $t_R$ ) to all image points by showing the corresponding wavefronts. For a time recording of backscattered energy at R due to source at S, so-called scattering traveltimes  $t_{SR} = t_S + t_R$  are needed at each



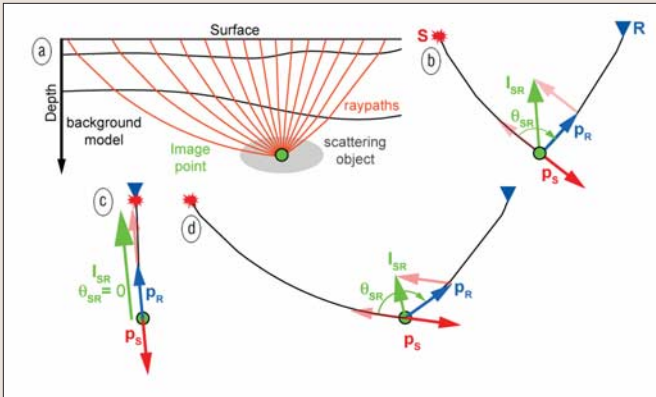
**Figure 3.** Scattering isochrones in PSDM. (a) Isotropic case: formation of elliptic scattering isochrones in a homogeneous model as the sum of two traveltime grids to get the scattering traveltime. These grids show circular wavefronts whose centers are shot S (red marker) and receiver R (blue triangle). S and R are the focal points of the elliptic scattering isochrones. (b) and (c) Anisotropic case: scattering isochrones in a homogeneous VTI model ( $V_p = 2500 \text{ m/s}$ ,  $V_s = 1000 \text{ m/s}$ ,  $\epsilon = 0.1$ ,  $\delta = -0.1$ ) for a PP scattering (b) and a PS scattering (c).



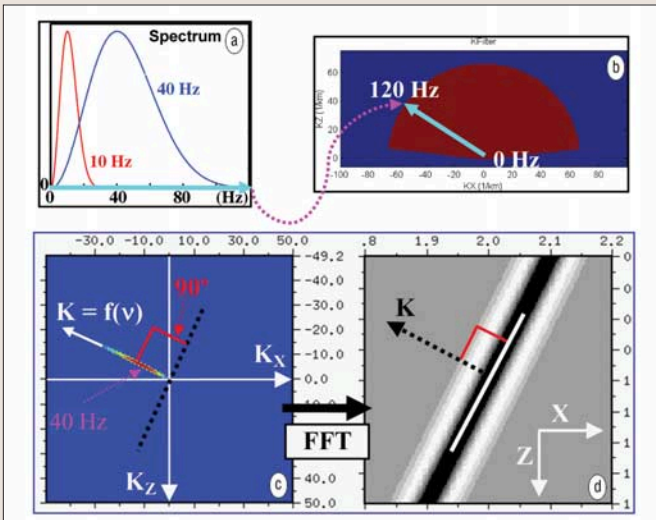
**Figure 4.** Scattering isochrones and PSDM. The background velocity model is homogeneous and isotropic. A point scatterer is located at the center of the image (yellow disk). Both a zero-offset survey (shot/receiver positions spread over 4 km) and a common-shot survey (one shot at 0 km and receivers along the same 4 km) are considered. (a) Zero-offset: PSDM image attached to one shot/receiver couple, i.e., the one just above the point scatterer. (b) Common-shot: PSDM image attached to one receiver at 3 km. (c) Zero-offset: PSDM image attached to the whole zero-offset survey. (d) Common-shot: PSDM image attached to the whole common-shot acquisition.

image point to relate seismic energy recording time to depth locations. The isolines of  $t_{SR}$  are called *scattering isochrones* and are elliptic in the homogeneous isotropic case. Some migration methods will explicitly calculate  $t_{SR}$  in the chosen velocity model (Kirchhoff), while others will do so implicitly when forward/back propagating wavefields in that velocity field, but in all cases, the scattering traveltime  $t_{SR}$  is the key to the depth imaging process. In more realistic models, the scattering isochrones are never elliptic and may take quite odd shapes, this effect being even worse when considering anisotropy and wave conversion (Figures 3b and 3c).

**PSDM.** If only one trace is used, i.e., one SR pair, the PSDM image will show nonzero amplitudes along and near the corresponding scattering isochrones (Figure 4). When S and R are at the same location (zero-offset) and above the point scatterer (Figure 4a), the PSDM image shows a circle, as expected from the corresponding scattering isochrone (sum of two circles with the same center). This circular pattern crosses the actual location of the point scatterer and has a



**Figure 5.** Illumination vector (isotropic case without wave conversion). (a) Model with an unknown scattering object around one considered image point. Raypaths are drawn to illustrate the propagation effect in the background model. (b) Local definition of the illumination vector  $I_{SR}$  as the difference of two slowness vectors, i.e.,  $p_R - p_S$ , where  $p_S$  is attached to the incident wave (from source S) and  $p_R$  to the scattered wave (toward receiver R).  $\theta_{SR}$  is the opening angle between  $-p_S$  and  $p_R$ . The orientation and size of  $I_{SR}$  depend on the considered source/receiver couple and the propagation effect in the overburden: (c) Zero  $\theta_{SR}$  case, i.e., longest  $I_{SR}$ . (d) Large  $\theta_{SR}$  case, i.e., small  $I_{SR}$ .



**Figure 6.** Scattering wavenumber vector ( $k_{SR}$ ) mapping. (a) Example of frequency spectrum used when mapping  $k_{SR}$ . (b) Wavenumber domain: the blue arrow indicates the direction along which the frequency spectrum will be mapped. This is the direction of the corresponding illumination vector  $I_{SR}$  (Figure 5). (c) Result of the mapping for the 40-Hz spectrum. The color along the  $I_{SR}$  direction indicates the amplitude of the spectrum (highest in red, i.e., at 40 Hz). (d) Result of applying a fast FT (FFT) to (c) to go to the space (depth) domain: a plane wavefront perpendicular to  $k_{SR}$ , hence to  $I_{SR}$  as well, is obtained and has a thickness depending both on the original length of  $I_{SR}$  and the considered frequency band.

constant thickness. If we now take another SR pair (Figure 4b), noncoincident this time, the PSDM image shows, as predicted, an elliptic pattern, but its thickness is larger than in the zero-offset case and varies all over the scattering isochrone. These elementary PSDM images are equivalent to the so-called *impulse response* of an imaging system. If we now take several traces, either in a zero-offset acquisition (Figure 4c), or as a common-shot recording (Figure 4d), the final PSDM image will result from a superposition of these elementary impulse responses, with constructive interference at the location of the point scatterer and, hopefully, destructive interference elsewhere. The final images resulting from that superposition are quite different between the

zero-offset and common-shot case, though it is the same point scatterer and the same emitted pulse. The question now is: Can we predict such results without first having to calculate the time recordings attached to a point scatterer at each image point, and without performing PSDM each time?

As demonstrated above, the final seismic image results from the superposition of elementary images obtained by spreading recorded backscattered energy along scattering isochrones for each SR pair. If enough properly sampled seismic traces are available, a constructive interference or focusing occurs at actual locations of point scatterers, while destructive interference attenuates or removes the rest. So PSDM itself provides a way to estimate PSF if we first generate synthetic data corresponding to chosen point scatterers and then depth-migrate these data. But this is a very costly process if PSFs at all image points of a chosen PSDM target are to be calculated. In addition, it may be difficult because it requires a proper modeling method. Such a combined modeling plus migration approach in PSF calculation is the only solution for a wave-equation type of migration. Asymptotic integral approaches (Kirchhoff) using ray-based precalculated Green's functions (traveltime, amplitudes, etc.) offer a more flexible and data-independent method to calculate PSFs. When first calculating Green's functions in a background velocity model, extra parameters can indeed be calculated at a low additional cost to extract key information for PSF, i.e., the scattering wavenumber vector  $K_{SR}$  (Hamran and Lecomte, 1993) derived from the illumination vector  $I_{SR}$ .

**Illumination and scattering wavenumber vectors.** The illumination vector  $I_{SR}$  is defined at a chosen image point and in a background velocity model (Figure 5a).  $I_{SR}$  is the difference of two local vectors,  $p_S$  and  $p_R$ , i.e.,  $I_{SR} = p_R - p_S$  (Figure 5b).  $p_S$  and  $p_R$  are the slowness vectors attached to the incident wavefield and the scattered wavefield, respectively.  $p_S$  and  $p_R$ , hence  $I_{SR}$ , are calculated by ray-tracing methods and similar (e.g., eikonal solvers) techniques, giving high-frequency approximations of the solutions of the wave equation (no frequency dependency). Without wave conversion, i.e., the incident wave is the same type as the scattered one (P- or S-wave),  $I_{SR}$  can be written as:

$$I_{SR} = p_R - p_S = \frac{(\hat{u}_R - \hat{u}_S)}{V} = \frac{2\cos(\theta_{SR}/2)}{V} \hat{u}_{SR} \quad (4)$$

where  $V$  is the velocity of the incident and scattered waves at the image point, and  $\hat{u}_S$  and  $\hat{u}_R$  are two unit vectors perpendicular to the incident wavefront from source S and to the scattered wavefront towards receiver R, respectively.  $\hat{u}_S$  and  $\hat{u}_R$  are always parallel to the raypath at the considered image point in isotropic cases (as in Figure 5) but not in anisotropic cases.  $\theta_{SR}$  is the opening angle between  $\hat{u}_R$  and  $-\hat{u}_S$  (Figure 5b). It will depend on the position of the SR pair with respect to the image point and on the wave propagation in the background model.  $\theta_{SR}$  plays a very important role in resolution, as will be seen, because it controls the length of  $I_{SR}$ . Note that when  $\theta_{SR}$  is equal to  $0^\circ$ , i.e.,  $\hat{u}_S = \hat{u}_R$  (normal-incidence backscattering, Figure 5c),  $I_{SR}$  is at its longest ( $2/V$ ), while when  $\theta_{SR}$  increases,  $I_{SR}$  gets shorter (Figure 5d). The extreme case is  $\theta_{SR} = 180^\circ$ , i.e.,  $\hat{u}_S = -\hat{u}_R$  and  $I_{SR} = 0$  (direct transmission).

The scattering wavenumber vector is easily derived from  $I_{SR}$  by multiplying it with the frequency  $v$ :

$$k_{SR} = vI_{SR} = v(p_R - p_S) = k_R - k_S = k_R \hat{u}_R - k_S \hat{u}_R \quad (5)$$

where  $k_S$  and  $k_R$  are two local plane wavenumbers, the first being attached to the incident wave and the second to the scattered wave. Therefore,  $\mathbf{k}_{SR}$  is parallel to  $\mathbf{I}_{SR}$  and has a length equal to the one of  $\mathbf{I}_{SR}$  multiplied by the frequency. But why do we need  $\mathbf{k}_{SR}$ ?  $\mathbf{k}_{SR}$  is a key component in resolution analysis because it defines a *local plane wavefront tangent to the scattering isochrone*,  $\mathbf{k}_{SR}$  being perpendicular to the latter (Lecomte and Gelius, 1998).  $\mathbf{k}_{SR}$  is the wavenumber-domain representation of that local plane wavefront (depth-domain), the two being connected by Fourier transform (FT). When mapped in the wavenumber domain and considering only one frequency, the corresponding image in the depth domain will be a monochromatic plane wavefront. This is similar to the time-frequency FT relation where one frequency corresponds to a sine in the time domain. When considering a frequency band, i.e., seismic band modulated by a pulse, the corresponding spectrum (Figure 6a) is mapped in the wavenumber domain along the direction of  $\mathbf{k}_{SR}$  (Figures 6b and c). The resulting image in depth is now a band-limited plane wavefront (Figure 6d).

Knowing  $\mathbf{I}_{SR}$  at an image point, hence  $\mathbf{k}_{SR}$ , means knowing the local shape of the corresponding scattering isochrone (Figure 7), not only its local geometry (tangent perpendicular to  $\mathbf{I}_{SR}$ ), but also its local thickness (inversely proportional to the length of  $\mathbf{k}_{SR}$ ). The latter explains why the PSDM image in Figure 4b (common-shot data) shows a thicker impulse response than in the zero-offset case (Figure 4a): The opening angle  $\theta_{SR}$  is larger, which in turn gives a shorter  $\mathbf{k}_{SR}$ , hence a longer signal in the depth domain (as also illustrated in Figures 5c and d). This is the well-known pulse-stretching effect in PSDM, increasing with increasing offsets caused by the widening of the opening angle  $\theta_{SR}$ , hence decreasing the length of  $\mathbf{I}_{SR}$  independently of the frequency band.

**Scattering wavenumber and PSF.** Once all  $\mathbf{k}_{SR}$  are calculated at one image point for a set of selected SR pairs, we obtain numerically an approximation of the local superposition of the scattering isochrones by first mapping all  $\mathbf{k}_{SR}$  in the wavenumber domain for a certain frequency band and pulse and then applying a Fourier transform to get the corresponding depth image (summation). The latter is the PSF attached to the considered image point and function of the selected SR pairs, frequency band, background velocity model, etc. As an example, Figure 8 shows the two PSFs calculated at the point-scatterer location of Figure 4 and for both survey selections. The PSFs exhibit very similar patterns in the vicinity of the point scatterer compared to those observed on the PSDM images (Figure 4), showing the validity of the ray-based approach. However, the local plane-wavefront approximation restricts the zone of validity of these PSFs to the vicinity of the considered image point. Both PSFs are characterized by a high-resolution (HR) and low-resolution (LR) axis, the first being parallel to the mean-scattering wavenumber vector and the second perpendicular to the latter. The HR axis defines the “cross-reflector” resolution, which would correspond to the “vertical” resolution mentioned in literature ( $\lambda/4$  being the critical value), while the LR axis defines the “lateral” resolution axis, which would correspond to the “horizontal” resolution (the Fresnel zone effect). However, it is easy to see from the PSF of the common-shot data set (Figure 8b) that the terms “vertical” and “horizontal” may not be appropriate, even in a simple homogeneous isotropic background velocity field (see Figure 2b).

The method discussed above is the proposed alternative approach used in the following to calculate PSF, i.e., without modeling point-scatterer data and migrating them. The

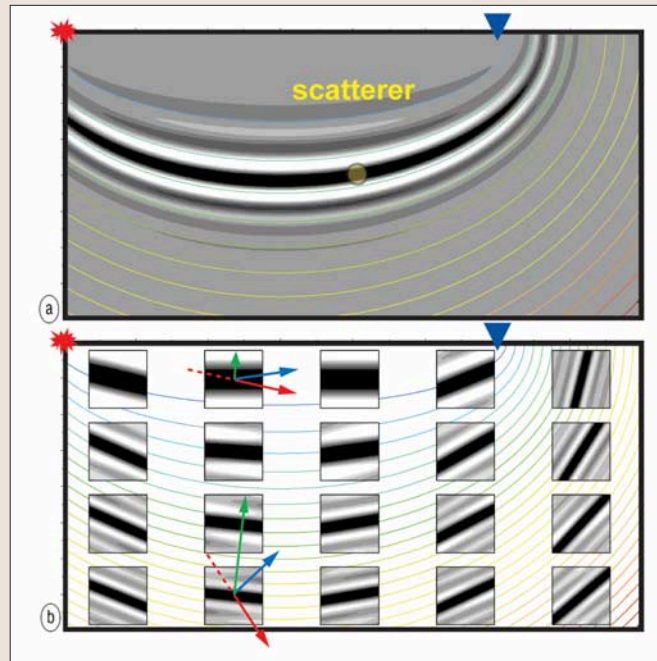


Figure 7. Illumination vector ( $\mathbf{I}_{SR}$ ) versus PSDM. (a) Mono-record PSDM image of Figure 4b. The corresponding scattering isochrones are superimposed. (b) Local plane-wavefront images (see Figure 6d) attached to some  $\mathbf{I}_{SR}$  and superimposed on the scattering isochrones. Two  $\mathbf{I}_{SR}$  are given (green arrows) with their corresponding slowness vectors  $\mathbf{p}_S$  (red arrow) and  $\mathbf{p}_R$  (blue arrow). Note how each small plane-wavefront image is locally tangent to the scattering isochrones. Note also the change in thickness of the plane wavefronts related to the change in length of  $\mathbf{I}_{SR}$  (same frequency band for all locations).

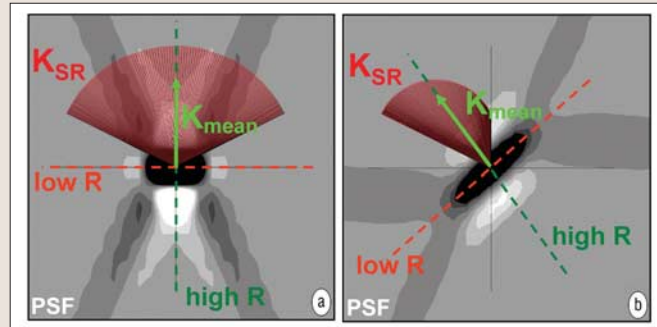


Figure 8. Scattering wavenumber vectors  $\mathbf{k}_{SR}$  superimposed on their corresponding PSF for the model used in Figure 4. (a) Zero-offset survey case. (b) Common-shot survey case. (a) and (b) are to be compared with Figures 4b and d at the location of the point scatterer, respectively. The mean  $\mathbf{k}_{SR}$  is also superimposed to show its relation to the orientation of the central lobe of the PSF. Along this vector, the resolution is at its highest (partly because of the frequency band of the pulse), while it is at its lowest perpendicular to it (Fresnel zone effect).

assumed Earth model  $\mathbf{G}$  (e.g., the one determined for PSDM) is used to calculate the scattering wavenumber vectors  $\mathbf{k}_{SR}$  with ray-based modeling methods. I considered an “acoustic” isotropic Earth model  $\mathbf{G}$  in the right side of Equation 4, without introducing wave conversion and anisotropy. The theory holds, however, for *elastic* models, *wave conversion*, and *anisotropy*, the important part of Equations 4 and 5 being that  $\mathbf{I}_{SR} = \mathbf{p}_R - \mathbf{p}_S$  and  $\mathbf{k}_{SR} = \mathbf{k}_R - \mathbf{k}_S$ , respectively. This means that

$$\mathbf{I}_{SR} = \mathbf{p}_R - \mathbf{p}_S = \frac{\hat{\mathbf{u}}_R}{V_{IP\_R}} - \frac{\hat{\mathbf{u}}_S}{V_{IP\_S}} \quad (6)$$

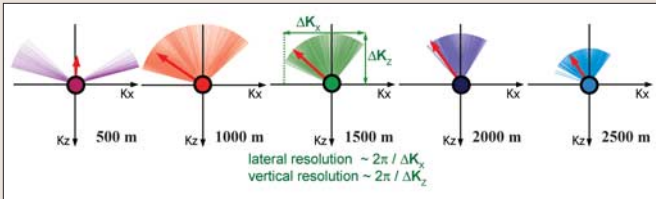


Figure 9. Marmousi model. Scattering wavenumber vector coverages corresponding to the PSF shown in Figure 2. The figures illustrate how to estimate roughly lateral and vertical resolution from such a plot.

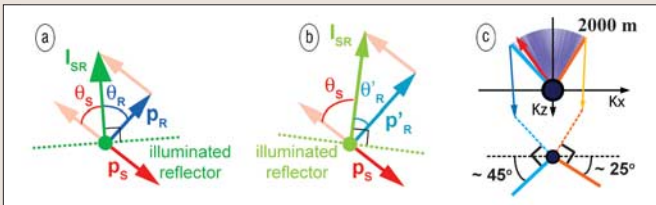


Figure 10. Relation between illumination vector  $I_{SR}$  (see Figure 5) and the corresponding potentially illuminated reflector, i.e., Snell's law (specular reflection), with  $I_{SR}$  parallel to the normal of the illuminated reflector. (a) No wave-conversion case, i.e., the two corresponding slowness vectors are of equal length  $\| p_S \| = \| p_R \|$ ; (b) wave-conversion case, i.e.,  $\| p'_R \| > \| p_S \|$  in the case of a PS conversion ( $S$ -velocity lower than  $P$ -velocity). Even if  $p'_R$  has the same orientation as  $p_R$ , the corresponding  $I_{SR}$  is different than in (a) in both orientation and length. (c) Scheme illustrating the determination of the range of illuminated reflector dips. The dip angle is equal to the angle between  $I_{SR}$  or  $k_{SR}$  and the vertical axis.

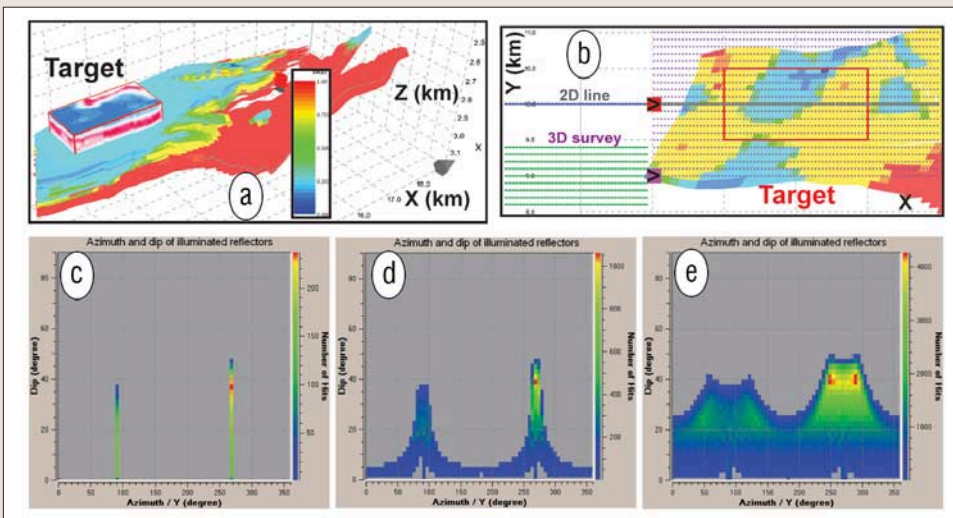


Figure 11. Norne reservoir model courtesy of StatoilHydro. (a) Location of a local PSDM target (cube) in the reservoir model (water saturation is used for the color mapping). (b) Location and geometry of the modeled surveys. 2D line (grey markers): the red square is the first shot and the blue line shows the streamer. 3D survey (magenta markers): the magenta square is the first shot and the green lines show the streamers. Illumination plots showing both dips and azimuths of the potentially illuminated reflectors at the center of the target with (c) the 2D monostreamer line, (d) a 2D multistreamer line (same multistreamer configuration as for the 3D survey), and (e) the 3D grid with multistreamer acquisition.

where  $V_{IP,S}$  and  $V_{IP,R}$  are the velocities at the image point (IP) attached to the incident wave (from S) and to the scattered wave (toward R), respectively. A "PP" scattering ( $V_{IP,S} = V_{IP,R} = V_p$ ) will therefore correspond to a shorter  $I_{SR}$  than an "SS" scattering ( $V_{IP,S} = V_{IP,R} = V_s$ ) because the velocity of the S-wave ( $V_s$ ) is smaller than the velocity of the P-wave ( $V_p$ ). An intermediate case is a "PS" scattering or "SP" scattering, i.e., with wave-conversion at the image point. In the

anisotropic case,  $\hat{u}_S$  and  $\hat{u}_R$  are still perpendicular to the wavefronts but are no longer necessarily parallel to the ray-paths. As long as ray-tracing and similar methods are able to calculate  $p_S$  and  $p_R$  in a 2D/3D background velocity field, including wave conversion in the elastic case and anisotropy, the PSF can be calculated at each image point. In the following, only the "PP" isotropic scattering case will be further discussed and illustrated ( $V_{IP,S} = V_{IP,R} = V$ ), but the extension to conversion and anisotropy is straightforward.

**Scattering wavenumber and resolution.** Considering the Fourier-transform relation between  $k_{SR}$  in the wavenumber domain and the PSF in the depth domain, we need a large scattering-wavenumber band to get a sharp PSF (hence good resolution). This is similar to the Fourier-transform relation between time domain and frequency domain in signal processing: An impulsive (short) pulse in time corresponds to a large frequency-band spectrum, the ideal case being a spike in time, that corresponds to a white-band spectrum in frequency. The coverage in the wavenumber domain will depend on orientation and length of  $k_{SR}$ . The orientation is controlled by the wave propagation in the Earth model, both for the incident and scattered wavefields, i.e., function of the Earth model  $G$ , the survey (set of SR pairs), and the wave type (P, S, different paths). The length of  $k_{SR}$  is proportional to the frequency, inversely proportional to the local velocity  $V$  at the image point, and will also reflect the opening angle  $\theta_{SR}$  between  $p_S$  and  $p_R$ . The larger the frequency band, the larger the zone covered in the wavenumber domain, hence sharper resolution. In an opposite manner, a larger local velocity induces a shorter wavenumber coverage, producing poorer resolution. This is a known problem for deep structures because seismic velocity is usually increasing with depth. Note that S-waves are more interesting because of their lower velocity (shorter wavelength), though they may suffer from attenuation. Similar to the velocity effect, the larger the opening angle  $\theta_{SR}$  (larger offset is the main reason), the shorter the wavenumber coverage, leading again to poorer resolution.

An estimation of "lateral" and "vertical" resolution can be deduced from the  $k_{SR}$  coverage (Figure 9) in the wavenumber domain attached to each PSF calculated in the Marmousi model (Figure 2). A flat band-limited spectrum was used to get the optimal resolution attainable within the considered frequency band.

**From point scatterers to reflectors.** How can we relate the PSF to PSDM images of reflecting structures since only point scatterers have been considered to this point? As is the case in the exploding reflector concept used in the modeling of zero-offset data, Huygens' principle can be used to approximate a reflector as a set of point scatterers, each acting as a secondary source when illuminated by an incident wavefield. The interference of all wavefields generated by the sec-

ondary sources will properly construct the reflector response, assuming a proper density of point scatterers along the reflector. Because each point scatterer (secondary source) will correspond to a scattering isochrone in PSDM, the reconstruction of the reflector in depth will result from the interference of all scattering isochrones, the final image of the reflector being the envelope.

Reflectors are imaged in PSDM if the scattering isochrones calculated in the Earth model are tangent to them. This is another way to express Snell's law, explaining *specular reflections*. Because  $I_{SR}$  is perpendicular to the scattering isochrone,  $I_{SR}$  must be parallel to the normal of the reflector being considered for the latter to be illuminated (Figure 10a). Note that this is also true in the case of wave conversion (Figure 10b). This means that the orientation of  $I_{SR}$  provides very important information (assuming that the Earth model  $G$  is the proper one!): the dip and azimuth of illuminated reflectors at and near the considered image point. It means that during survey planning, one can predict which reflectors will be illuminated, without acquiring any data and knowing anything about the actual scattering structure in the target (at least in detail, because some of it is in the background model in the form of a smooth velocity field inside the target of interest). Dip information can be extracted from the  $I_{SR}$  or  $k_{SR}$  plots in the Marmousi model (Figure 10c), i.e., getting the corresponding illuminated reflectors by taking a  $90^\circ$  rotation of the extreme  $I_{SR}$  or  $k_{SR}$ .

**Survey effect.** Once the illumination vectors  $I_{SR}$  are calculated, it is easy to produce local illumination maps at a chosen image point. A reservoir model of the Norne Field (Norwegian continental shelf), courtesy of StatoilHydro, is selected to illustrate this point (Figure 11a). A homogeneous background velocity model was used, and three surveys were considered when calculating  $I_{SR}$ . The chosen image point is at the center of the 3D PSDM target (Figure 11a, 2.65 km in depth), i.e., vertically below the 2D line (Figure 11b). Instead of plotting the corresponding  $I_{SR}$  like in Figure 9, the dip and azimuth of the potentially illuminated reflectors are calculated and plotted in a simple rectangular plot for each case. For the 2D mono-streamer survey, only reflectors with an azimuth parallel to the acquisition line are illuminated, i.e., with an azimuth of  $90^\circ$  with respect to the y-axis (x-line direction) in the sailing direction (inline), and an azimuth of  $90^\circ + 180^\circ = 270^\circ$  in the opposite direction (Figure 11c). The dip range is asymmetric because of the intrinsic half-spread of a marine line, i.e., covering less dips ( $0-48^\circ$ ) in the sailing direction of the boat than in the opposite one due to the streamer length ( $0-55^\circ$ ). For the 2D line with multistreamers, a wider range of azimuths is illuminated (Figure 11d), the range being even wider for the 3D grid (Figure 11e). A homogeneous background velocity was used here to emphasize the survey effect, but in real cases this velocity field also plays a major role in illumination and resolution.

**Overburden effect.** The background velocity model has indeed a marked effect on illumination (Figure 12a). If the 3.5 km-deep flat reflector is the target, points A and B should be equivalent in terms of reflectivity and reflector shape (the latter is influencing the illumination). However, because point A is below a relatively simple overburden with flat layering, while B is below a salt body, the wave propagation will be significantly different between sources/receivers and A and B. As a consequence, the  $k_{SR}$  are different (Figure 12b). Point A is relatively well illuminated (dips from  $0^\circ$  to about  $45^\circ$  on both sides), which results in a nice PSF, i.e., the image of a point scatterer at A (Figure 13b). On the contrary,

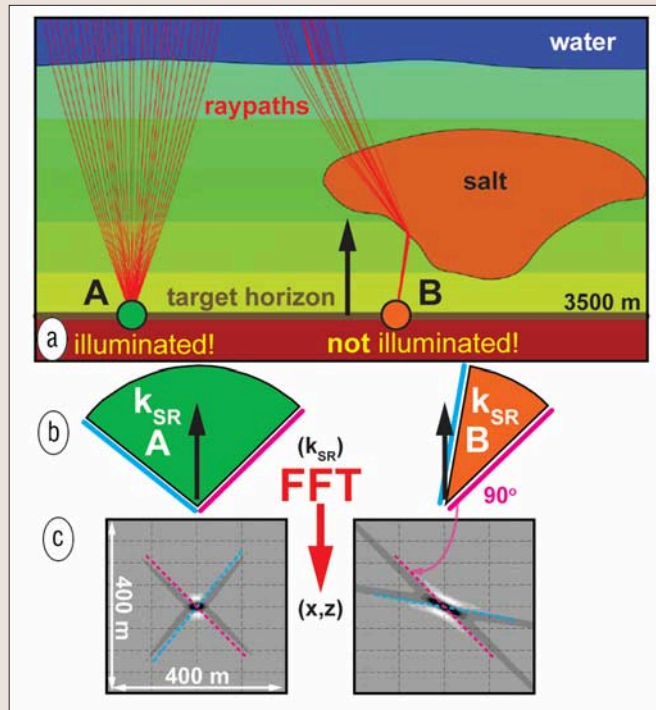


Figure 12. Overburden effect. (a) 2D background velocity model, with a flat target reflector partly below a salt body and location of two reference points A and B. (b) Scattering wavenumber vector  $k_{SR}$  coverages for both points. The normal to the reflector (black arrow) is covered at A (illumination) but not at B (no illumination). (c) Corresponding PSF for A and B with explanation of the relation between the observed cross-pattern on the PSF and the extreme  $k_{SR}$  of the ranges given in (b) (dashed magenta and blue lines).

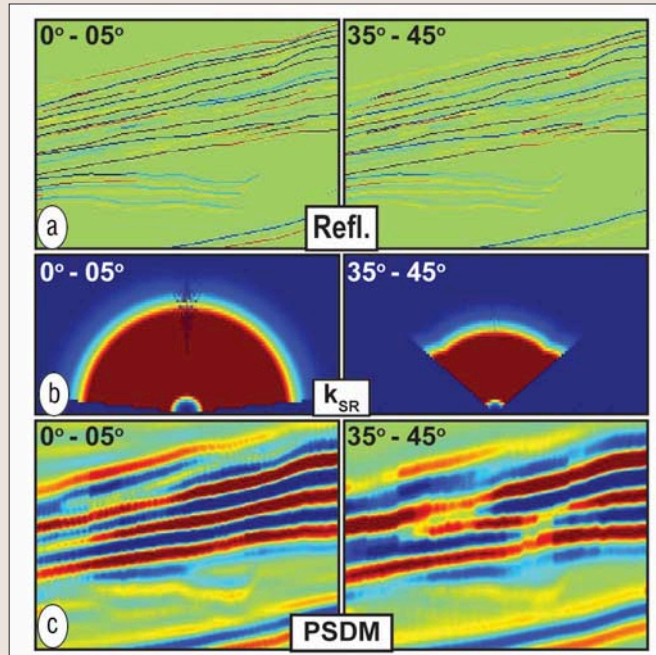


Figure 13. Angle-dependency effects on both reflectivity grids (a) and scattering wavenumber vectors (b) for small (left) and large (right) incidence-angle ranges. (c) Corresponding PSDM images resulting from both effects. The reservoir model used for the reflectivity is the Storvola model courtesy of Svalex.

point B is poorly illuminated, with a asymmetry in  $k_{SR}$  (Figure 13a), i.e., reflectors with dips toward the left, including the horizontal ones and low dips toward the right are

not illuminated. The horizontal target horizon should therefore not appear near B on the PSDM image. However, a point scatterer at B will be imaged, but with strong distortions (Figure 13b).

**Angle dependency.** Having now related the orientation of  $I_{SR}/k_{SR}$  to potentially illuminated reflectors, the opening angle  $\theta_{SR}$  (Figure 5) can be decomposed into two angles,  $\theta_S$  and  $\theta_R$  (Figures 10a and b), i.e., the incident angle  $\theta_S$  between  $p_S$  and  $I_{SR}$  and the scattered angle  $\theta_R$  between  $p_R$  and  $I_{SR}$ , with  $\theta_{SR} = \theta_S + \theta_R$ . With reference to Figure 10a,  $\theta_S$  can also be called the *incidence angle* attached to the specular reflection at a reflector perpendicular to  $I_{SR}$  at the considered image point, though we do not know whether or not such a reflector is present in the actual structure. However, if there is a reflector at that image point,  $\theta_S$  and  $\theta_R$  are following Snell's law, e.g.,  $\theta_{SR} = \theta_R$  in a nonconversion mode (PP or SS). This observation is crucial to explain the incidence-angle dependency in PSDM images.  $k_{SR}$  can be sorted in terms of angle ranges instead of offset selection. This is important because the reflectivity of the target is strongly dependent on the incidence angle (AVO/AVA effect). There is a link between reflectivity,  $k_{SR}$  and PSDM images (Figure 13). The  $k_{SR}$  coverage is changing for different incidence-angle ranges, with very good illumination for the small angles (nearly perfect with all dips) and more limited illumination for the large angles, with additionally a coarser cross-reflector resolution caused by the larger opening angle. Therefore, the corresponding PSDM images result from a combination of angle-dependent reflectivity and angle-dependent illumination/resolution.

As suggested previously, many parameters influence the illumination and resolution in a background PSDM velocity model, for a given survey, etc. The calculation of the illumination vectors  $I_{SR}$ , which leads to the scattering wavenumber vectors  $k_{SR}$  leading to PSF, has proven to be an important step toward a better understanding of PSDM images. But this only gives "expert" information which is not necessarily easy to handle. A major step forward is the development of a method which takes into account the PSF to simulate PSDM images.

**A PSDM simulator.** Classically, there are two approaches to simulate seismic images. The first one is a typical modeling workflow consisting of modeled synthetic traces that are processed to get a final migrated image. This approach is difficult and expensive. The second is a significant shortcut, and is currently the favorite in the oil industry. This method (hereafter referred to as *1D convolution*) requires simulating the final migrated image by convolution of vertical reflectivity profiles with a wavelet. The method is easy to understand and to program and is common within the industry. However, 1D convolution is strictly valid for layered models with no lateral velocity variations, a requirement that is far from the case in the subsurface. Moreover, 1D convolution only approximates poststack time-migrated data.

Having developed an efficient numerical tool to get PSF at any image point in a target area, a PSDM simulator has been implemented, that acts as a 3D prestack depth convolution method. The method is called *simulated prestack local imaging* (SimPLI) (Norway patent 322089, U.S. patent granted). SimPLI makes use of the model-resolution Equation 3, i.e., applying the calculated ray-based PSF in a background velocity model to the reflectivity of a superimposed target (e.g., reservoir). This is done by either convolution in the depth domain, or multiplication in the

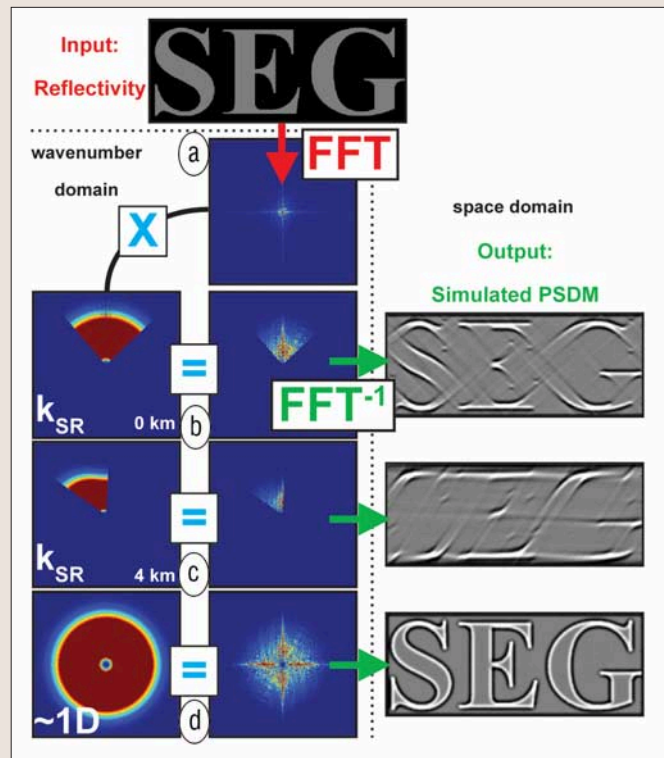
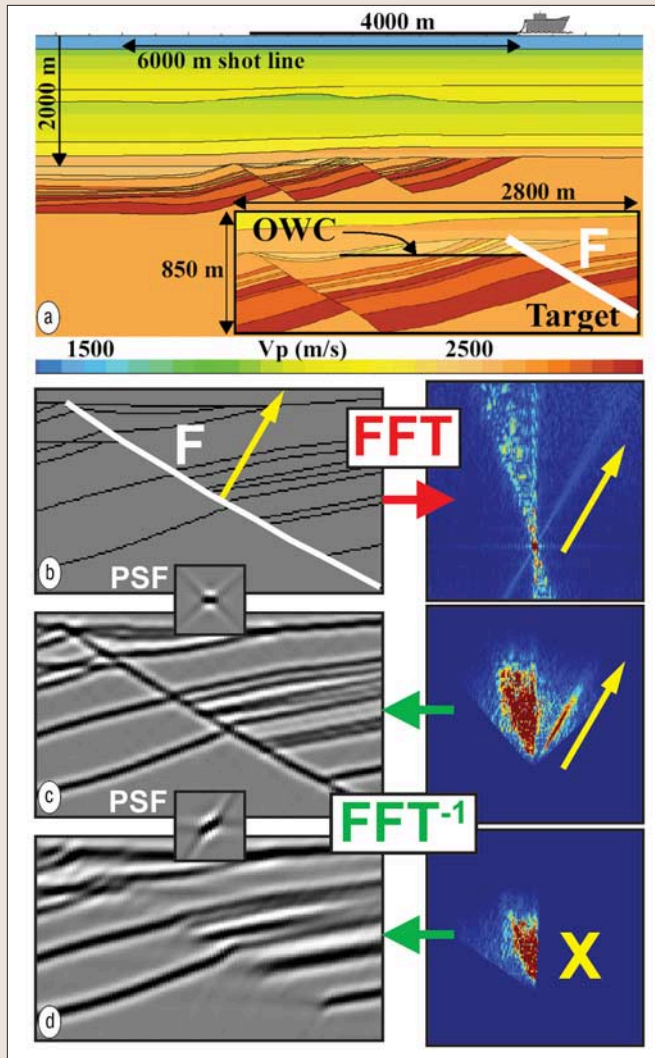


Figure 14. Illumination and resolution effects on the SEG logo. (a) SEG logo taken in as input to the PSDM simulator and transformed to the wavenumber domain. (b) Simulated PSDM for a near-offset selection. (c) Simulated PSDM for a far-offset selection. (d) Simulation of 1D convolution effect. (b), (c), and (d) show from left to right the corresponding wavenumber filter, then the result of applying that filter to the SEG logo, still in the wavenumber domain, and finally the resulting simulated PSDM image in the space (depth) domain.

wavenumber domain, and using fast FT (FFT) to perform the depth-to/from-wavenumber conversions. SimPLI acts as a signal- or image-processing method, distorting the actual reflectivity to reproduce the effects of seismic imaging. This is comparable to what is done in PSDM, where a seismic data set is used to retrieve the unknown reflectivity (only a filtered version, as suggested earlier). This distorted reflectivity is superimposed by PSDM to the (smooth) background velocity field used for the propagation effects (traveltimes). In the simulator approach, which is a modeling one, we know the reflectivity in depth, so there is no need for the back propagation of the migration method, but we simulate instead the focusing effect (imaging) by distorting the true reflectivity according to the PSF. In the following, the result of the mapping of  $k_{SR}$  in the wavenumber domain will be called a *wavenumber filter* to emphasize the image-filtering approach.

To illustrate the PSDM simulator (Figure 14), let me first consider the SEG logo as the input reflectivity grid, which is then transformed to the wavenumber domain (Figure 14a). Using ray tracing in a given background model, two wavenumber filters were obtained for two constant-offset survey selections and a 20-Hz zero-phase Ricker wavelet (Figures 14b and c, left). These filters are then applied in the wavenumber domain to the input reflectivity grid and finally an inverse FFT gives the simulated PSDM images (Figures 14b and c, right). The SEG logo is distorted as a result. The zero-offset image is best but it is missing the steep contours of the characters. The PSDM simulator can also be used to simulate a 1D convolution for the sake of comparison (Figure 14d). A 1D-convolution simulator corresponds to a per-



**Figure 15.** PSDM simulator on a synthetic 2D model of the Gullfaks Field, courtesy of StatoilHydro. (a) Synthetic model with survey and target. A background velocity model containing the overburden and a smooth field in the target has been used to calculate the wavenumber filters already used in Figures 14b (zero-offset) and c (large-offset). In the following figures (b to d), images will be given in both space and wavenumber domain. (b) Reflectivity grid extracted around a fault F (normal indicated by a yellow vector). (c) Simulated PSDM result obtained when using the zero-offset filter. (d) Simulated PSDM result obtained when using the large-offset filter. In (c) and (d), the corresponding PSF is given at the top of the spatial image. Note the disappearance of the fault in (d) caused by a lack of illumination vectors parallel to the normal, i.e., the filter removed the fault signal (parallel to the yellow arrow) in the wavenumber domain.

fect illumination of all reflector dips and azimuths, which is equivalent to a circular wavenumber filter (Figure 14d, left). A cross-reflector resolution effect is introduced by taking into account the band-limited pulse. However, no lateral resolution effects (Fresnel zones) can be reproduced due to the circular shape of the filter. As a result, the obtained SEG logo image is not realistic, showing all “dips” with just a certain thickness of the contours (Figure 14d, right).

To illustrate the PSDM simulator in a more realistic model, a 2D example in a synthetic model of the Gullfaks Field (Norwegian continental shelf) is used (Figure 15). In the target of interest, showing a fault, a constant-reflectivity grid is extracted for the sake of illustration. If we assume that the PSFs within that target are only slightly varying all over the zone, the PSF calculated at the center of the target

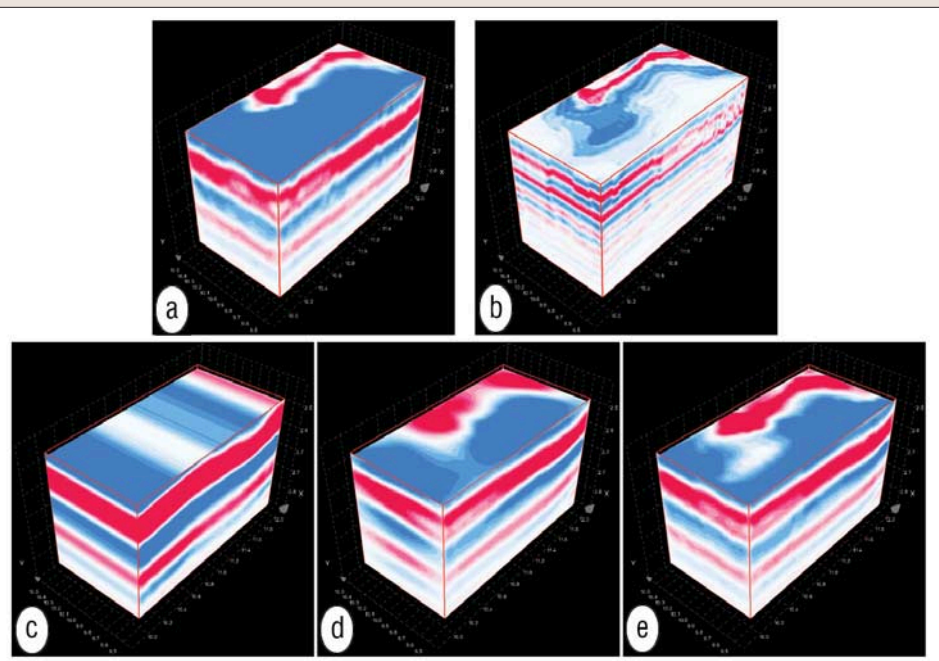


**Figure 16.** Norne reservoir model examples with simulated PSDM cubes for the target and surveys given in Figure 11. Frequency-band effects when using the 3D survey: (a) 20 Hz and (b) 40 Hz. Survey effects when using a 20-Hz pulse: (c) 2D line, monostreamer. (d) 2D line, multistreamer and (e) 3D survey. The horizontal slice in (c) to (e) is slightly deeper than the one in (a) and (b). The inline direction is along  $x$ .

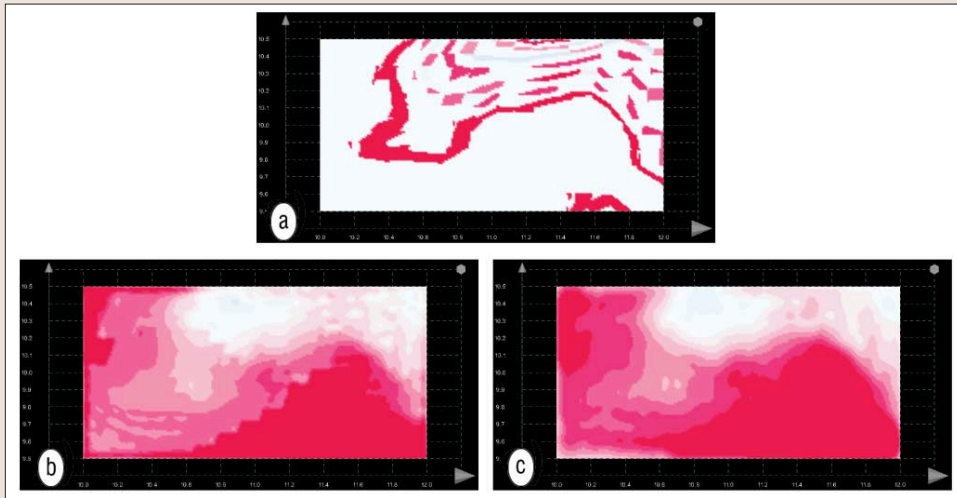


**Figure 17.** Norne reservoir model example with 1D versus PSDM simulator comparisons for one horizontal slice in the target of Figure 11. (a) Reflectivity. (b) Simulated 1D-convolution. (c) PSDM simulator.

may be used all over the grid and the process is easily done in the wavenumber domain. In Figure 15, the wavenumber filters of Figures 14b and c are used, corresponding to a 2D varying background velocity field in Gullfaks. This example illustrates two major effects described earlier: illumination effect on the fault (imaged with zero offset but not with the chosen large offset) and decrease in resolution because of larger opening angles in the large-offset selection.

**Examples.** The Norne model is used in the following to simulate PSDM cubes (Figure 16). The reservoir model was given in Eclipse format and rock physics transformations were applied to get the elastic parameters necessary to calculate the reflectivity in the target. A homogeneous background velocity field is used to focus on effects other than

the overburden. Figures 16a and b show the pulse-dependency on the resolution: the longer the frequency band, the sharper the resolution. Figures 16c through e show survey effects on the simulated PSDM cubes. The total lack of crossline resolution with the monostreamer 2D line is clearly visible (Figure 16c), though simplified here because of the local plane-wavefront approximation attached to the use of  $\mathbf{k}_{SR}$ . Curvature parameters from ray tracing should be used to correct for the plane-wavefront effect. However, it is clear that 3D images should not be obtained from pure 2D acquisition. It is only when first introducing multistreamers (Figure 16d) and then 3D surveys (Figure 16e), that crossline resolution appears.

Finally, another comparison is presented between 1D-convolution (the standard method) and the PSDM simulator which is indeed a 3D prestack space convolution, hence an extension of the convolution principle in seismic modeling (Figure 17). As in Figure 14d, the 1D convolution is simulated here in depth. A proper comparison would consist of either depth conversion of 1D time-simulated images, or time conversion of simulated depth images, though without considering the post-stack / prestack difference between the two simulation approaches. This comparison is done in the 3D target on one horizontal slice. The reservoir model being obtained from an Eclipse file, the reflectivity cubes/ grids are inherently quite coarse due to the large pillars of the Eclipse file (reservoir modeling grid), though sampled down to 10 m horizontally and 2.5 m vertically (bi-linear interpolation) (Figure 17a). As a consequence, the reflectivity clearly shows square patterns in the horizontal slice. The illumination being perfect in the 1D-like filter, the corresponding PSF is quite sharp, having just the limited frequency-band effect of the pulse. As a consequence, the horizontal slice shows the contours of the Eclipse pillars (Figure 17b). On the contrary, the PSDM-like filter, corresponding to the actual illumination of the structure, introduces the actual lateral-smoothing effect (Fresnel zone) and the image is thus smoother, giving a more appropriate rendering of a seismic PSDM section (Figure 17c).

**Conclusions.** Ray-based approaches allow an efficient and flexible calculation of illumination vectors (difference of two local slowness vectors) at any image point in an imag-

ing target, as a function of the survey, background velocity model, pulse, and wave phases. This can be done in isotropic and anisotropic media in complex background models, and wave conversion can be included. The illumination vector alone gives fundamental information in terms of dip and azimuth of potentially illuminated reflectors (the actual reflectors are not known). Each illumination vector corresponds to one potentially illuminated reflector: the one perpendicular to the illumination vector (Snell's law). However, it is possible to go much further by introducing a frequency dependency to form the scattering wavenumber vectors. A mapping of the latter in the wavenumber domain will give the point-scatterer function (PSF), hence resolution of the PSDM system, after taking a Fourier transform to get back to the depth domain. This approach is data-independent, i.e., the illumination and resolution capabilities of a given combination of survey, model, pulse, and wave types can be calculated prior to any PSDM migration of actual data.

Considering reflectors as sets of point scatterers acting as secondary sources in reflection seismic (Huygens' principle), and knowing through the PSF (space-domain) or their corresponding scattering-wavenumber filters (wavenumber domain) how a point scatterer is imaged in PSDM, an efficient PSDM simulator has been developed. It works as a 3D prestack space-convolution method applying calculated 3D PSFs to 3D reflectivity cubes (FFT-based image-processing approach). This goes far beyond the standard 1D poststack time-convolution seismic simulators used in industry, adding proper 3D illumination and resolution effects, including angle-dependency of both reflectivity and PSF. Though key approximations are done here, such as the local plane-wavefront approximation in the calculation of the PSFs, and the use of the same PSFs for a size-limited reflectivity cube (target-oriented local imaging), extensions are possible. The first consists of considering curvature parameters calculated by ray tracing to extend the plane-wave approximation to higher-order approximations. The second consists of a space-dependent convolution where the PSFs are precalculated at the nodes of a cube and interpolated to get a better PSF estimate for each image point. However, the space-variant convolution is more time-consuming and an alternative is to use the actual local process in an iterative mode for several local adjacent targets, merging all resulting PSDM cubes at the end. Such a process is easy to parallelize on a multinode machine or on a cluster of computers.

The actual version of the PSDM simulator is working in

a "true-amplitude" mode, i.e., all scattering wavenumber vectors are attached with the same weight when mapping in the wavenumber domain. However, it is easy to consider other parameters calculated by ray tracing, such as traveltime, amplitude, attenuation, polarization, etc., to modify these weights and thus introduce various effects on the simulated PSDM results. These could be amplitude effects (especially to study some ad hoc corrections functions of traveltimes), directivity pattern for both source and receiver, attenuation in the background model, and decomposition of the wavefield for multicomponent receivers (polarization needed).

**Suggested reading.** *Seismic Resolution: A Quantitative Analysis of Resolving Power of Acoustical Echo Techniques* by Berkhoult (Geophysical Press, 1984). *Geophysical Data Analysis: Discrete Inverse Theory* by Menke (International Geophysics Series, 45, 1989). "Have a look at the resolution of prestack depth migration for any model, survey and wavefields" by Lecomte and Gelius (SEG 1998 *Expanded Abstracts*). "Analysis of the resolution function in seismic prestack depth imaging" by Gelius et al. (*Geophysical Prospecting*, 2001). "Improved applicability of ray tracing in seismic acquisition, imaging, and interpretation" by Gjøystdal et al. (*GEOPHYSICS*, 2007). "Local and controlled prestack depth migration in complex areas" by Lecomte (*Geophysical Prospecting*, 1999). "Improving Kirchhoff migration with repeated local plane-wave imaging; a SAR-inspired signal-processing approach in prestack depth imaging" by Lecomte et al. (*Geophysical Prospecting*, 2005). "Simulated 2D/3D PSDM images with a fast, robust, and flexible FFT-based filtering approach" by Lecomte and Pochon-Guerin (SEG 2005 *Expanded Abstracts*). "Simulating migrated and inverted seismic data by filtering a geologic model" by Toxopeus et al. (*GEOPHYSICS*, 2008). **TLE**

**Acknowledgments:** This work has been supported by the Research Council of Norway through several projects over the last ten years (131341/420, 128440/43, and 153889/420). The author thanks NORSAR for the authorization to publish the present paper, and all NORSAR and NORSAR Innovation colleagues for their contribution and support, especially for the development of the SeisRoX software utilizing the SimPLI PSDM simulator. The author also thanks Rick Miller for his help. NORSAR thanks StatoilHydro (geo- and Eclipse models), IFP (Marmousi data), Seismic Unix, and the "Svalex" project ([www.svalex.net](http://www.svalex.net), Storvola Eclipse model).

**Corresponding author:** [isabelle@norsar.no](mailto:isabelle@norsar.no)